Transactions on Control Systems Technology

Threat-based hazard avoidance for semi-autonomous vehicles using nonlinear model predictive control

Journal:	*IEEE Transactions on Control Systems Technology*
Manuscript ID:	Draft
mstype:	Regular Paper
Date Submitted by the Author:	n/a
Complete List of Authors:	Peters, Steven; MIT, Mechanical Engineering Anderson, Sterling; MIT, Mechanical Engineering Pillutti, Tom; Ford Motor Company, Research and Advanced Engineering Tseng, Eric Iagnemma, Karl; MIT, Mechanical Engineering
Keywords:	active safety, autonomous systems, hazard avoidance, human-in-the-loop, model predictive control, semi-autonomous control, threat assessment, vehicle autonomy

Threat-based hazard avoidance for semi-autonomous vehicles using nonlinear model predictive control

Steven C. Peters, Sterling J Anderson, Tom Pilutti, H. Eric Tseng, Karl Iagnemma

***Abstract*-- Passenger vehicle accidents cause thousands of deaths, millions of injuries, and hundreds of billions of dollars in damage in the United States every year. At this time, driver error is a significant factor in a majority of vehicle accidents. To mitigate driver error, a semi-autonomous hazard avoidance system is proposed based on shared control between a human driver and autonomous vehicle navigation system. Given measurements of vehicle states and hazard locations, the system rapidly plans a safe trajectory and associated control inputs using a vehicle model with nonlinear model predictive control. The threat to the vehicle is computed based on the nearness to handling limits of a predicted trajectory. Control authority is switched between the driver and automated system based on the predicted threat. The computational requirements of the controller are reduced by computing an approximate threat based on canonical avoidance trajectories. Simulation and experimental results with steering and braking control demonstrate successful hazard avoidance, while allowing driver control in low-threat situations.**

***Index Terms*--active safety, autonomous systems, hazard avoidance, human-in-the-loop, model predictive control, semi-autonomous control, threat assessment, vehicle autonomy.**

I. Introduction

SIGNIFICANT research and development effort over the past 40 years has been devoted to improving the safety of passenger vehicles. This work has led to the development of passive safety systems, such as seat belts, air bags, optimized crush zones, and active safety systems, such as anti-lock brakes and electronic stability control. Those systems have effected measurable reductions in U.S. motor vehicle accident rates [1, 2]. Despite these efforts, more than 40,000 people were killed and 2.5 million injured in motor vehicle accidents in the United States in 2004, at an estimated economic cost of $200 billion [3].

Reactive stability control systems intervene via steering and braking actuators when skidding or wheel lift-off is detected. These systems react to the current vehicle state and are designed to function in concert with driver inputs. While reactive systems are effective in reducing accident rates [2], they do not consider the effect of driver error, such as rear-end collisions with an obstacle or drifting off the road. The impact of driver error is nontrivial, as it has been found to be the primary cause of 60% of motor vehicle accidents and a contributing factor in 95% of accidents [4].

One approach to mitigating the problem of driver error in accident causation is to develop crash avoidance control systems with some autonomy. Perception and navigation for autonomous vehicles has been studied extensively by robotics researchers, with the recent DARPA Urban Challenge representing the state of the art [5, 6, 7]. Despite recent advances in autonomous vehicle technology, however, barriers of public perception currently limit its widespread commercialization. Many drivers are uncomfortable relinquishing control of their vehicle to a "computer." For these drivers, semi-autonomous systems, which allow some degree of driver autonomy, may be desirable.

Lookahead sensors have been deployed in non-safety-critical automotive systems such as Adaptive Cruise Control. A recent system used on Ford and Volvo vehicles uses lookahead sensing to trigger emergency braking in certain scenarios to prevent collisions or reduce collision severity [8]. There are, however, no systems currently on the market that detect and prevent collisions using steering actuators at high speed.

Several systems for obstacle avoidance and automotive lane-keeping with a human-in-the-loop have been proposed using potential fields. A lane-keeping system for a passenger vehicle based on potential fields with steering handwheel force feedback is proposed in [9]. Bounds on the lateral vehicle position are provided based on the potential field and a linear model of vehicle sideslip dynamics [10]. This approach to lane keeping with potential fields does not suffer from local minima because it does not consider longitudinal vehicle dynamics.

Another proposed shared control system uses a potential

Manuscript received December 9, 2010. (Write the date on which you submitted your paper for review.) This work was supported in part by Ford Motor Company.

Steven C. Peters, Sterling J Anderson, and Karl Iagnemma are with the Department of Mechanical Engineering, Massachusetts Institute of Technology, Cambridge, MA 02139 USA (phone: 617-452-3262; fax: 617-258-5802, e-mail: scpeters [at] mit [dot] edu, ster [at] mit [dot] edu, kdi [at] mit [dot] edu).

Tom Pilutti and Eric Tseng are with Research and Innovation Center, Ford Research Laboratories, Dearborn, MI 48124 USA (e-mail: tpilutti@ford.com; htseng@ford.com).

field over an environment containing obstacles and the motion planning construct known as "elastic bands" to generate a desired path for a semi-autonomous controller to track [11]. The system described in [11] cannot guarantee obstacle avoidance, however. While the systems described in [9, 10, 11] address obstacle avoidance through lateral positioning, further work is needed to address the avoidance of obstacles through both lateral and longitudinal control.

Computational demands are typically quite significant for high-speed hazard avoidance systems. A motion planning technique for high-speed hazard avoidance based on cellular decomposition and the concept of trajectory space was proposed in [12]. The method was developed to minimize computational overhead at the expense of optimality of the resulting motion plan.

Another promising approach for real-time planning in the presence of hazards is based on numerical optimization with constraint satisfaction. Mixed integer linear programming (MILP) was used by Richards, Kuwata, and How [13] in a receding horizon controller to navigate a vehicle with linear dynamics around obstacles. The avoidance of rectangular obstacles was ensured by constraints on integer variables. An approximate cost-to-go was also used to account for uncertainty beyond a limited detection horizon. The resulting controller executes in real-time and was demonstrated experimentally. Nonlinear programming was used by Eele and Richards [14] to plan shortest hazard-free paths for a "Dubins-like" car with nonlinear dynamics. The avoidance of circular obstacles was ensured with nonlinear constraints. The computational burden was reduced through a branch-and-bound optimization. Nonlinear model predictive control (MPC) was used by Falcone, et al. [15] to generate a path-tracking controller for an automobile operating near the tire friction limits. The controller was demonstrated experimentally at speeds up to 21 m/s on icy roads.

Linear model predictive control has been used in previous work by the authors [16, 17] to prevent departure of a vehicle with linearized vehicle dynamics from a predefined, hazard-free corridor. The corridor constraints were encoded as time-varying constraints on the lateral vehicle position. This controller was incorporated into a threat-based semi-autonomous system and demonstrated experimentally. The limitations of this work stem primarily from the model linearization, which required a constant speed assumption.

This paper presents an active safety system for hazard avoidance that allows drivers full control authority in benign situations, but intervenes when danger is significant. Such a system is termed a semi-autonomous hazard avoidance system. A block diagram of the proposed system is shown in Fig. 1. Look-ahead sensing devices and a perception system generate a map of drivable terrain surfaces and hazards around the vehicle. A model predictive controller for motion planning and control uses this map, as well as driver input and vehicle state measurements, to continuously determine control inputs that ensure that the vehicle avoids hazards and loss of control over a forward-looking time horizon. A threat assessment algorithm determines the danger of a given situation based on the dynamic feasibility of future trajectories and switches control authority between the driver and vehicle system, such that during low threat scenarios, the driver is given full control authority, while during high threat scenarios, the control authority is shared between the driver and the hazard avoidance controller.

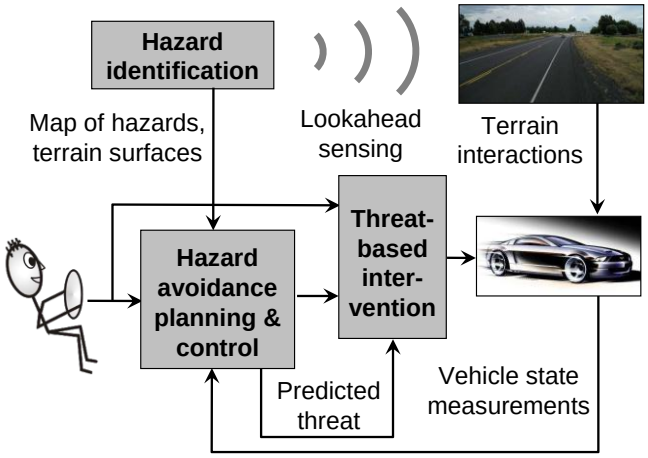

Fig. 1. Semi-autonomous hazard avoidance system design.

Hazard avoidance trajectories and corresponding control inputs are computed by a nonlinear model predictive controller. The controller is designed to minimize the threat of the resulting hazard avoidance trajectories. The use of nonlinear MPC enables the use of a nonlinear model of both longitudinal and lateral vehicle dynamics, allowing improved performance relative to previous work based solely on lateral vehicle dynamics [16, 17].

The computational demands of nonlinear MPC impose a significant challenge for real-time implementation. An approach to mitigating excessive computational requirements is to incorporate an approximation of the cost function as a cost-to-go, as in [13]. A contribution of this paper is a computationally efficient method for estimating threat, which is used as a cost-to-go to reduce the computational demand of the MPC optimization.

A brief outline of the paper is as follows. In Section II, the subsystems of the semi-autonomous hazard avoidance system are described, including the vehicle model, model predictive controller, method for computing threat, and threat-based intervention strategy. In Section III, the performance of the system is shown via simulation and experimental results, followed by a discussion of the results in Section IV.

II. Semi-autonomous hazard avoidance system description

This section describes the model predictive controller that is used for both threat assessment and collision avoidance control in the proposed semi-autonomous hazard avoidance system.

A. Nonlinear vehicle model

A nonlinear bicycle model used in the model predictive controller is presented here and illustrated in Fig. 2. The vehicle states include the c.g. position [*X*,*Y*], body-fixed velocity components v_x and v_y, yaw angle ψ and yaw rate $\dot{\psi}$. The vehicle has mass *m* and yaw inertia I_{zz}. The c.g. position relative to the front and rear wheels is specified by parameters x_f and x_r. The controllable inputs consist of the front steering angle δ and the longitudinal tire forces F_{xf} and F_{xr}, which are controlled via braking actuators. Lateral tire friction forces act at the front and rear wheels and are denoted F_{yf} and F_{yr}, respectively.

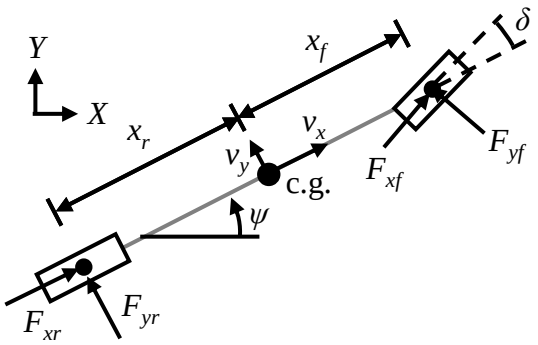

Fig. 2. Planar bicycle model.

The vehicle dynamics are given by momentum conservation equations as:

$$\begin{bmatrix} m(\dot{v}_x - v_y\dot{\psi}) \\ m(\dot{v}_y + v_x\dot{\psi}) \\ I_{zz}\ddot{\psi} \end{bmatrix} = \begin{bmatrix} \cos\delta & -\sin\delta & 1 & 0 \\ \sin\delta & \cos\delta & 0 & 1 \\ x_f\sin\delta & x_f\cos\delta & 0 & -x_r \end{bmatrix} \begin{bmatrix} F_{xf} \\ F_{yf} \\ F_{xr} \\ F_{yr} \end{bmatrix} \quad (1)$$

The lateral tire forces F_{yf} and F_{yr} are functions of the tire slip angles α_f and α_r, as $F_{yf}(\alpha_f)$ and $F_{yr}(\alpha_r)$. The slip angles α_f and α_r are illustrated in Fig. 3 and are computed as:

$$\alpha_f = \tan^{-1}\left(\frac{v_y + x_f\dot{\psi}}{v_x}\right) - \delta \quad (2)$$

$$\alpha_r = \tan^{-1}\left(\frac{v_y - x_r\dot{\psi}}{v_x}\right) \quad (3)$$

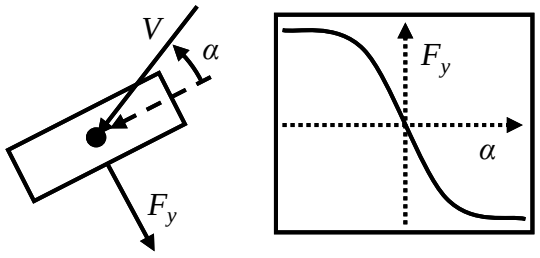

Fig. 3. Lateral tire friction force model. The slip angle α is the angle between the velocity vector at the wheel center and the longitudinal axis of the tire. The lateral tire force F_y opposes lateral slip.

It is assumed that the longitudinal braking forces F_{xf} and F_{xr} are proportionally controlled by a single input u_{brake}, as is common for braking systems. The proportion of braking applied at the front wheel is given by $b_f \in [0,1]$ as follows:

$$F_{xf} = b_f u_{brake} \quad (4)$$

$$F_{xr} = (1 - b_f)u_{brake} \quad (5)$$

Input rate constraints are also assumed, so that the steering and braking inputs are controlled via integral control as follows:

$$\dot{\delta} = u_1 \quad (6)$$

$$\dot{u}_{brake} = u_2 \quad (7)$$

The vehicle model is expressed in nonlinear state space form $\dot{\mathbf{x}} = f(\mathbf{x},\mathbf{u})$ with input vector $\mathbf{u} \equiv [u_1\ u_2]^T$ and state vector $\mathbf{x} \equiv [X\ Y\ \psi\ v_x\ v_y\ \dot{\psi}\ \ \delta\ u_{brake}]^T$.

$$\dot{\mathbf{x}} = \begin{bmatrix} v_x\cos\psi - v_y\sin\psi \\ v_x\sin\psi + v_y\cos\psi \\ \dot{\psi} \\ v_y\dot{\psi} + \frac{1}{m}\left[(1 + b_f(\cos\delta - 1))u_{brake} - F_{yf}(\alpha_f)\sin\delta\right] \\ -v_x\dot{\psi} + \frac{1}{m}\left(b_f u_{brake}\sin\delta + F_{yf}(\alpha_f)\cos\delta + F_{yr}(\alpha_r)\right) \\ \frac{1}{I_{zz}}\left(x_f b_f u_{brake}\sin\delta + x_f F_{yf}(\alpha_f)\cos\delta - x_r F_{yr}(\alpha_r)\right) \\ u_1 \\ u_2 \end{bmatrix} \quad (8)$$

The steering and braking inputs are subject to magnitude and rate constraints given below.

$$|\delta| \le \delta_{\max} \quad (9)$$

$$-u_{brake,\max} \le u_{brake} \le 0 \quad (10)$$

$$|\mathbf{u}| \le \mathbf{u}_{\max} \quad (11)$$

The friction forces at the front and rear tires are also subject to friction circle constraints given below, where μ is the surface friction coefficient, F_{zf} is the normal contact force at the front wheels, and F_{zr} is the normal contact force at the rear wheels.

$$\sqrt{F_{xf}^2 + F_{yf}^2} \le \mu F_{zf} \quad (12)$$

$$\sqrt{F_{xr}^2 + F_{yr}^2} \le \mu F_{zr} \quad (13)$$

For this work, the effect of longitudinal load transfer is not considered. The normal contact forces are computed based on the static load transfer distribution as follows:

$$F_{zf} = \frac{x_r}{x_f + x_r} mg \quad (14)$$

$$F_{zr} = \frac{x_f}{x_f + x_r} mg \quad (15)$$

B. Hazard geometry

The *N* hazards in the environment are represented by polygons P_1, P_2, .., P_N. Each hazard polygon P_i consists of n_i nodes $\mathbf{p}_{ij}$, $j \in 1\text{-}n_i$. For this work, all hazards are assumed to be fixed, though moving hazards could be considered if the displacement and orientation of each hazard as a function of

time was known or could be estimated.

An example scene is given in Fig. 4, with road edges represented by P_1 and P_2 and a hazard represented by P_3. The vehicle geometry is approximated as a circle of radius r that is centered at point c. It is assumed that point c lies on the centerline of the vehicle a distance x_c from the vehicle c.g., as shown on the right side of Fig. 4. The parameters x_c and r should be chosen so that the front corners of the vehicle are within the circle but without exaggerating the vehicle width. For forward travel, a single circle may suffice for approximating the vehicle shape.

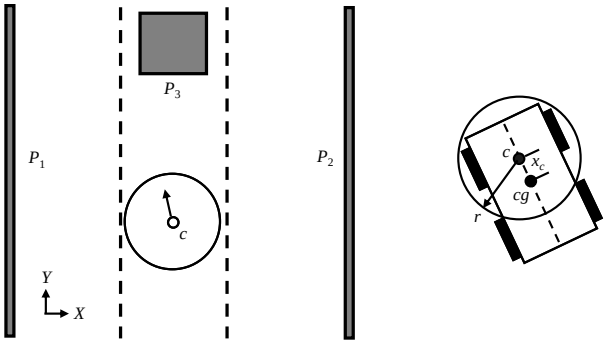

Fig. 4. Example hazard avoidance scenario. Road edge hazards are given as polygons P_1, P_2 and an additional hazard in the road P_3. The vehicle is approximated by a circle of radius r at point c.

If the minimum distance from point c to the nearest hazard polygon is given by $h(\mathbf{x})$, hazard avoidance can be assured by maintaining a clearance of at least r between point c and the nearest hazard polygon.

The model parameters used in this paper are given below in Table I.

TABLE I
VEHICLE MODEL PARAMETERS

Description	Symbol	Value
Mass	m	2220 kg
Yaw inertia	I_{zz}	3344 kg m^2
Front axle from c.g.	x_f	1.432 m
Rear axle from c.g.	x_r	1.472 m
Clearance point	x_c	0.10 m
Clearance radius	r	0.90 m
Steering angle limit	δ_{max}	10 deg
Steering rate limit	$u_{1,max}$	40 deg/s
Braking force limit	$u_{brake,max}$	19600 N
Braking rate limit	$u_{2,max}$	1.31e6 N/s
Brake bias	b_f	0.507

C. Threat definition and approximation

Threat arises from constraints on actuation and mobility that may make a hazard unavoidable. For example, a vehicle traveling at speed V at distance D from a fixed hazard requires an acceleration of V^2 / (2D) to stop before colliding with the hazard. If this required acceleration exceeds the maximum allowable acceleration imposed by braking actuator limits and the tire surface friction limits, the vehicle will be unable to stop in time to avoid a collision. In a similar manner, a vehicle performing a constant radius turn of radius R to avoid an obstacle requires an acceleration of V^2 / R. An existing method for threat assessment is computed as the percentage of the maximum allowable acceleration required to avoid by stopping or a constant radius turn as described in [18].

The nonlinear vehicle model presented in the previous section is subject to input magnitude and rate constraints from (9)-(11), as well as friction circle constraints at the front and rear from (12)-(13). Thus, each constraint represents a source of threat. The constraints are normalized into the form shown below.

$$J_k(\mathbf{x}_i, \mathbf{u}_i) \le 1 \tag{16}$$

Threat can be computed for a candidate hazard avoidance trajectory by evaluating the values $J_k(\mathbf{x}_i,\mathbf{u}_i)$ for the states and inputs of that trajectory. A scalar value of the threat is computed as the norm of the predicted threat values. The peak value (ie. infinity norm) of each J_k is taken to represent the threat arising from each constraint [19].

An approximation of threat is presented below that is used for a computationally-efficient cost-to-go. Although the steering angle constraint restricts low-speed turning, the tire friction constraints are more often the limiting factor in hazard avoidance at higher speeds. The front friction force is usually more controllable than the rear, since there is typically no rear-wheel steering control. Additionally, previous studies have found the front friction constraint to be more critical to understeering or plow out than the rear friction constraint [15]. For these reasons, the threat approximation is here based on the front friction circle constraint only.

A useful tool for analyzing the properties of the front friction constraint is the decoupling of lateral and yaw dynamics using the method described by Ackerman in [20]. This decoupling is demonstrated below with a simplified form of the momentum relations from (1), where a_y is the lateral vehicle c.g. acceleration, and f_{yf} and f_{yr} are the front and rear lateral tire forces represented in a body-fixed frame rather than a tire-fixed frame. This simplified form is inverted to yield an expression for the tire forces f_{yf} and f_{yr} in terms of vehicle acceleration components.

$$\begin{bmatrix} ma_y \\ I_{zz}\ddot{\psi} \end{bmatrix} = \begin{bmatrix} 1 & 1 \\ x_f & -x_r \end{bmatrix} \begin{bmatrix} f_{yf} \\ f_{yf} \end{bmatrix} \tag{17}$$

$$\begin{bmatrix} f_{yf} \\ f_{yr} \end{bmatrix} = \frac{m}{x_f + x_r} \begin{bmatrix} x_r\left(a_y + \frac{I_{zz}}{mx_r}\ddot{\psi}\right) \\ x_f\left(a_y - \frac{I_{zz}}{mx_f}\ddot{\psi}\right) \end{bmatrix} \tag{18}$$

Recall from kinematics that the quantity $a_y + dx\ddot{\psi}$ is the lateral acceleration of a point on a rigid body at a distance dx in front of the c.g. Thus according to (18), the front and rear lateral tire forces are proportional to the lateral acceleration at specific points on the vehicle. These points are termed "decoupling points" as the lateral acceleration of these points

is proportional to one of the lateral tire forces f_{yf} or f_{yr} and decoupled from the other force. The point lying a distance $\frac{I_{zz}}{mx_r}$ in front of the vehicle c.g. is decoupled from the rear force f_{yr} and its lateral acceleration is proportional to the front force f_{yf}. The longitudinal acceleration a_{xp} and lateral acceleration a_{yp} at this point are given below.

$$\begin{bmatrix} a_{xp} \\ a_{yp} \end{bmatrix} = \begin{bmatrix} a_x - \frac{I_{zz}}{mx_r}\dot{\psi}^2 \\ a_y + \frac{I_{zz}}{mx_r}\ddot{\psi} \end{bmatrix} \tag{19}$$

If longitudinal forces in a body-fixed frame f_{xf} and f_{xr} are allocated between the front and rear wheels based on the load distribution so that the relation given below is satisfied, then the front friction constraint in (12) maps to the constraint given in (21).

$$f_{xf} - f_{xr} = \frac{x_r - x_f}{x_f + x_r} m a_x \tag{20}$$

$$\sqrt{\left(a_{xp} + \frac{I_{zz}}{mx_r}\dot{\psi}^2\right)^2 + a_{yp}^2} \le \mu g \tag{21}$$

The front friction constraint in (21) is approximated by a constraint on the magnitude of the acceleration vector in (19). This approximation is reasonable when the term $\frac{I_{zz}}{mx_r}\dot{\psi}^2$ is small. This approximation implies that the acceleration of simple geometric avoidance maneuvers such as constant radius turns can approximate the threat arising from the front friction constraint.

The decoupled point has position $[X_{pm},Y_{pm}]$ and velocity $[\dot{X}_{pm},\dot{Y}_{pm}]$ in a global frame. These states are used to compute simple geometric avoidance maneuvers and are given as follows:

$$\begin{bmatrix} X_{pm} \\ Y_{pm} \end{bmatrix} = \begin{bmatrix} X \\ Y \end{bmatrix} + \frac{I_{zz}}{mx_r}\begin{bmatrix} \cos\psi \\ \sin\psi \end{bmatrix} \tag{22}$$

$$\begin{bmatrix} \dot{X}_{pm} \\ \dot{Y}_{pm} \end{bmatrix} = \begin{bmatrix} \cos\psi & -\sin\psi \\ \sin\psi & \cos\psi \end{bmatrix}\begin{bmatrix} v_x \\ v_y + \frac{I_{zz}}{mx_r}\dot{\psi} \end{bmatrix} \tag{23}$$

For simplicity, it is assumed that one edge of a hazard polygon has been identified as the critical edge to be avoided. This corresponds to several types of scenarios involving avoidance of a single obstacle. Three canonical constant acceleration maneuvers that avoid a single hazard edge are now described: straight-line stopping, constant radius non-passing turn, and constant radius passing turn. The maneuvers are illustrated in Fig. 5 and are used in II.D. to approximate cost-to-go in the MPC computation. The minimum threat maneuver is computed as the candidate maneuver with the minimum required acceleration.

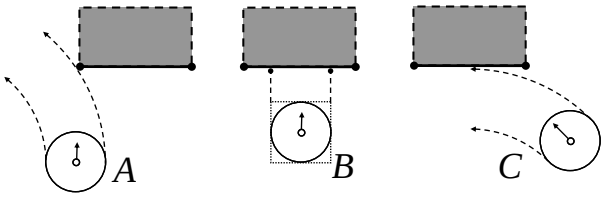

Fig. 5. Simple avoidance maneuvers. A passing maneuver is illustrated in part *A*, a stopping maneuver in part *B*, and a non-passing maneuver in part *C*.

1) Hazard avoidance during straight-line stopping

A straight-line stopping maneuver consists of acceleration applied in direct opposition to the vehicle velocity vector, causing the vehicle to stop before reaching the hazard *P*, as illustrated in Fig. 5 and Fig. 6. The critical edge of *P* is specified by nodes $\mathbf{n}_1$ and $\mathbf{n}_2$, tangent unit vector $\mathbf{e}_1$, and normal unit vector $\mathbf{e}_2$. For this maneuver, the vehicle is approximated as the bounding square surrounding the circle of radius *r* centered at point $[X_{pm},Y_{pm}]$. The square is to be parallel to the velocity unit vector $\mathbf{e}_4$ with front corner points $\mathbf{v}_1$ and $\mathbf{v}_2$.

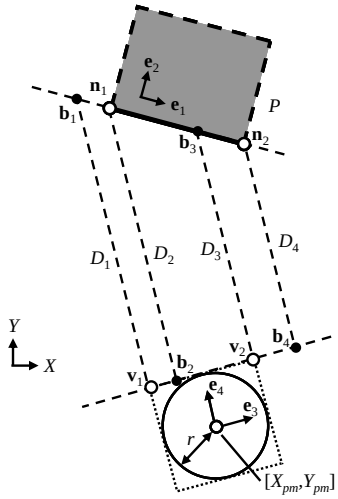

Fig. 6. Straight-line stopping maneuver. The critical edge of hazard *P* is specified by nodes $\mathbf{n}_1$, $\mathbf{n}_2$, and the vehicle is approximated by a square oriented with the vehicle velocity vector.

Possible points of collision $\mathbf{b}_1$-$\mathbf{b}_4$ are computed by projecting nodes $\mathbf{v}_1$, $\mathbf{v}_2$ along the velocity vector onto the hazard edge line and nodes $\mathbf{n}_1$, $\mathbf{n}_2$ along the velocity vector onto the vehicle edge line. The lines passing through nodes $\mathbf{n}_1$, $\mathbf{n}_2$ and $\mathbf{v}_1$, $\mathbf{v}_2$ are given below, where the components of unit vectors $\mathbf{e}_2$ and $\mathbf{e}_4$ are (e_{2x},e_{2y}) and (e_{4x},e_{4y}) and the coordinates of nodes $\mathbf{n}_1$ and $\mathbf{v}_1$ are (n_{1x}, n_{1y}) and (v_{1x}, v_{1y}).

$$e_{2x}(x - n_{1x}) + e_{2y}(y - n_{1y}) = 0 \tag{24}$$

$$e_{4x}(x - v_{1x}) + e_{4y}(y - v_{1y}) = 0 \tag{25}$$

The projection lines for computing points $\mathbf{b}_1$-$\mathbf{b}_4$ are computed as follows, where (x_i,y_i) are coordinates of the point to be projected:

$$e_{4y}(x - x_i) - e_{4x}(y - y_i) = 0 \tag{26}$$

The coordinates of a point $\mathbf{b}_i$ given by (b_{ix},b_{iy}) are computed by solving linear equations. For example, the

coordinates of point $\mathbf{b}_1$ are computed by solving the following:

$$\begin{bmatrix} e_{2x} & e_{2y} \\ e_{4y} & -e_{4x} \end{bmatrix} \begin{bmatrix} b_{1x} \\ b_{1y} \end{bmatrix} = \begin{bmatrix} e_{2x}n_{1x} + e_{2y}n_{1y} \\ -e_{4x}v_{1y} + e_{4y}v_{1x} \end{bmatrix} \quad (27)$$

Distances D_1-D_4 represent the projected distances of points $\mathbf{b}_1$-$\mathbf{b}_4$ and are computed as follows:

$$D_1 = \mathbf{e}_4 \cdot (\mathbf{b}_1 - \mathbf{v}_1) \quad (28)$$

$$D_2 = \mathbf{e}_4 \cdot (\mathbf{n}_1 - \mathbf{b}_2) \quad (29)$$

$$D_3 = \mathbf{e}_4 \cdot (\mathbf{b}_3 - \mathbf{v}_2) \quad (30)$$

$$D_4 = \mathbf{e}_4 \cdot (\mathbf{n}_2 - \mathbf{b}_4) \quad (31)$$

A projected point $\mathbf{b}_i$ lies outside of its projected line segment, e.g. points $\mathbf{b}_1$ and $\mathbf{b}_4$ in Fig. 5, if the following conditions are met:

$$\min\{\mathbf{e}_1 \cdot (\mathbf{b}_i - \mathbf{n}_1) < 0, \quad \mathbf{e}_1 \cdot (\mathbf{n}_2 - \mathbf{b}_i) < 0\} < 0 \qquad i \in \{1,3\} \quad (32)$$

$$\min\{\mathbf{e}_3 \cdot (\mathbf{b}_i - \mathbf{v}_1) < 0, \quad \mathbf{e}_3 \cdot (\mathbf{v}_2 - \mathbf{b}_i) < 0\} < 0 \qquad i \in \{2,4\} \quad (33)$$

For each projected point $\mathbf{b}_i$ that lies outside of its projected line segment, the corresponding distance D_i is set to infinity. The acceleration required by this stopping maneuver is computed as a_1 below, where D is taken to be the smallest of distances D_1-D_4. Note that if the vehicle will avoid the obstacle when traveling straight, the stopping distance will be infinity and its stopping acceleration will be zero.

$$a_1 = \frac{\dot{X}_{pm}^2 + \dot{Y}_{pm}^2}{2D} \quad (34)$$

2) Hazard avoidance during non-passing turn

A non-passing turn is defined as a constant radius turn in which the vehicle turns to travel parallel to the critical edge of a hazard *P*, as illustrated in Fig. 5 and Fig. 7 and described in this section. In contrast, a passing turn is defined as a constant radius turn in which the vehicle turns to pass the critical edge of hazard *P* to the left or the right, as described in the subsequent section and illustrated in Fig. 5 and Fig. 8. For example, non-passing turns can be used in a lane-keeping task or prevention of road departure.

The critical edge of *P* is specified by nodes $\mathbf{n}_1$ and $\mathbf{n}_2$, tangent unit vector $\mathbf{e}_1$, and normal unit vector $\mathbf{e}_2$. The vehicle is approximated as a circle of radius *r* centered at point $[X_{pm}, Y_{pm}]$ with velocity unit vector $\mathbf{e}_4$. The center is projected along unit vector $\mathbf{e}_3$ to the circumference of the circle to form points $\mathbf{v}_1$ and $\mathbf{v}_2$.

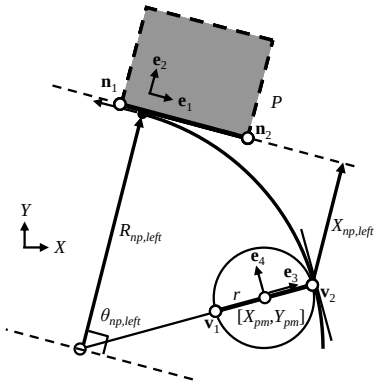

Fig. 7. Constant radius non-passing turn to the left. The critical edge of hazard *P* is specified by nodes $\mathbf{n}_1$, $\mathbf{n}_2$, and the vehicle is approximated as a circle of radius *r*.

A circle corresponding to a non-passing left turn with radius $R_{np,left}$ is defined by the following properties:

1. circle passes through point $\mathbf{v}_2$
2. circle is parallel to $\mathbf{e}_4$ at point $\mathbf{v}_2$
3. circle is tangent to line connecting $\mathbf{n}_1$ and $\mathbf{n}_2$
4. center of circle is to left of vehicle

The radius $R_{np,left}$ is computed as shown below based on intermediate values $\theta_{np,left}$ and $X_{np,left}$.

$$\cos\theta_{np,left} = -\mathbf{e}_1 \cdot \mathbf{e}_4 \quad (35)$$

$$X_{np,left} = (\mathbf{n}_1 - \mathbf{v}_2) \cdot \mathbf{e}_2 \quad (36)$$

$$R_{np,left} = \frac{X_{np,left}}{1 - \cos\theta_{np,left}} \quad (37)$$

A similar circle is found corresponding to a non-passing right turn based on point $\mathbf{v}_1$ with radius $R_{np,right}$ and intermediate values $\theta_{np,right}$ and $X_{np,right}$.

$$\cos\theta_{np,right} = \mathbf{e}_1 \cdot \mathbf{e}_4 \quad (38)$$

$$X_{np,right} = (\mathbf{n}_2 - \mathbf{v}_1) \cdot \mathbf{e}_2 \quad (39)$$

$$R_{np,right} = \frac{X_{np,right}}{1 - \cos\theta_{np,right}} \quad (40)$$

The larger of the two radii is termed R_{np}, and the corresponding turning acceleration a_2 is computed as shown below.

$$a_2 = \frac{\dot{X}_{pm}^2 + \dot{Y}_{pm}^2}{R_{np} - r} \quad (41)$$

3) Hazard avoidance during passing turn

A constant radius passing turn consists of acceleration perpendicular to the point mass velocity vector, causing the vehicle to turn and pass one of the nodes of hazard *P* as illustrated in Fig. 5 and Fig. 8. The critical edge of *P* is specified by nodes $\mathbf{n}_1$ and $\mathbf{n}_2$, tangent unit vector $\mathbf{e}_1$, and normal unit vector $\mathbf{e}_2$. For this maneuver, the vehicle is approximated as a circle of radius *r* centered at point $[X_{pm}, Y_{pm}]$ with velocity unit vector $\mathbf{e}_4$. The center is projected along unit vector $\mathbf{e}_3$ to the circumference of the circle to form points $\mathbf{v}_1$ and $\mathbf{v}_2$.

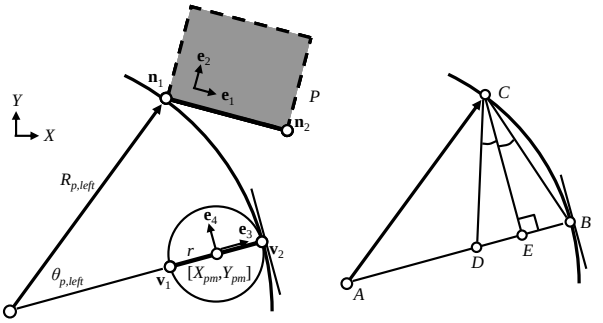

Fig. 8. Constant radius passing turn to the left. The critical edge of hazard *P* is specified by nodes $\mathbf{n}_1$, $\mathbf{n}_2$, and the vehicle is approximated as a circle of radius *r*. A set of similar triangles are illustrated in the right side of the figure.

A circle corresponding to a left passing turn with radius $R_{p,left}$ is defined by the following properties:

1. circle passes through point $\mathbf{v}_2$
2. circle is parallel to $\mathbf{e}_4$ at point $\mathbf{v}_2$
3. circle passes through node $\mathbf{n}_1$

The turn radius $R_{p,left}$ is computed with the aid of the triangles illustrated in the right side of Fig. 7. Points *B* and *C* correspond to points $\mathbf{v}_2$ and $\mathbf{n}_1$, respectively. Edge lengths $\overline{AB}$ and $\overline{AC}$ are both equal to the radius $R_{p,left}$. Since angles $\angle ECB$ and $\angle ECD$ are equal, it can be seen that triangle ΔCDB is isosceles. It can further be seen that triangles ΔABC and ΔCDB are similar. This similarity implies the following ratio:

$$\frac{\overline{AC}}{\overline{BC}} = \frac{\overline{CB}}{\overline{DB}} \tag{42}$$

Since edge length $\overline{AC}$ is equal to the unknown radius $R_{p,left}$, this ratio can be used to find an expression for the radius. Intermediate values $X_{p,left}$ and $Y_{p,left}$ are defined as follows:

$$X_{p,left} \equiv \overline{CE} = (\mathbf{n}_1 - \mathbf{v}_2)\cdot \mathbf{e}_4 \tag{43}$$

$$Y_{p,left} \equiv \overline{BE} = (\mathbf{v}_2 - \mathbf{n}_1)\cdot \mathbf{e}_3 \tag{44}$$

Using the following relations, an equation for the radius is found:

$$\overline{DB} = 2\overline{BE} = 2Y_{p,left} \tag{45}$$

$$\overline{CB} = \sqrt{\overline{BE}^2 + \overline{CE}^2} = \sqrt{X_{p,left}^2 + Y_{p,left}^2} \tag{46}$$

$$R_{p,left} = \frac{\overline{CB}^2}{\overline{DB}} = \frac{X_{p,left}^2 + Y_{p,left}^2}{2Y_{p,left}} \tag{47}$$

The angle $\theta_{p,left}$ can be found using the following relations:

$$\angle BCE = \tan^{-1}\frac{Y_{p,left}}{X_{p,left}} \tag{48}$$

$$\theta_{p,left} = \angle CAB = 2\angle BCE \tag{49}$$

A similar circle with radius $R_{p,right}$ is found corresponding to a right turn based on points $\mathbf{v}_1$ and $\mathbf{n}_2$ using intermediate values $X_{p,right}$ and $Y_{p,right}$.

$$X_{p,right} = (\mathbf{n}_2 - \mathbf{v}_1)\cdot \mathbf{e}_4 \tag{50}$$

$$Y_{p,right} = (\mathbf{n}_2 - \mathbf{v}_1)\cdot \mathbf{e}_3 \tag{51}$$

$$R_{p,right} = \frac{X_{p,right}^2 + Y_{p,right}^2}{2Y_{p,right}} \tag{52}$$

$$\theta_{p,right} = 2\tan^{-1}\frac{Y_{p,right}}{X_{p,right}} \tag{53}$$

The larger of the two radii is termed R_p, and the corresponding turning acceleration a_3 is computed as shown below.

$$a_3 = \frac{\dot{X}_{pm}^2 + \dot{Y}_{pm}^2}{R_p - r} \tag{54}$$

It should be noted that when starting far from the corner node of a hazard, the circular passing arc may cross the hazard edge in order to intersect the corner node, as shown in Fig. 9. When this occurs, a passing turn in that direction is not feasible. A condition for the feasibility of a passing turn is that the passing turn angle $\theta_{p,left}$, $\theta_{p,right}$ is less than the corresponding non-passing turn angle $\theta_{np,left}$, $\theta_{np,right}$. When passing turns are infeasible, a non-passing turn or stopping maneuver may be chosen instead.

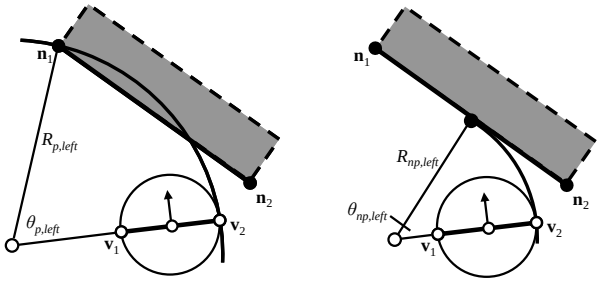

Fig. 9. Infeasible constant radius passing turn to the left. The vehicle is too far from the corner nodes to pass successfully. A non-passing turn may be attempted instead.

4) Summary

The threat associated with the front tire friction constraint is shown to be closely approximated by the acceleration of a "decoupling point" located in front of the c.g. This approximation is used to estimate the threat of several hazard avoidance maneuvers based on stopping and turning. The acceleration required for each of the three candidate maneuvers is computed. The maneuver with the smallest required acceleration is chosen as the maneuver representing the minimum threat maneuver.

The hazard avoidance maneuvers described in this section are constructed for stationary hazards. The maneuvers can be adapted to consider moving hazards by estimating the hazard trajectory based on the current hazard state and computing the future time and state of the hazard at which avoidance will occur as in [21].

D. Minimum threat hazard avoidance with MPC

In the previous section, threat was defined as the nearness to actuation limits of a hazard avoidance trajectory. A model predictive controller is defined here to compute hazard avoidance trajectories that minimize threat over a finite time

horizon. MPC is chosen for its use of a predictive model as well as its enforcement of inequality constraints. Inequality constraints are useful for considering actuator magnitude limits and ensuring clearance from hazards.

The model prediction consists of p steps with a discrete time step of t_s. The inputs $\mathbf{u}_i$, applied to the system over the prediction horizon, comprise the free variables used as optimization parameters. The optimization parameters are ordered in a single column vector $\mathbf{U}$.

$$\mathbf{U} = \begin{bmatrix} \mathbf{u}_0^T & \mathbf{u}_1^T & \dots & \mathbf{u}_{p-2}^T & \mathbf{u}_{p-1}^T \end{bmatrix}^T \tag{55}$$

Given the inputs in $\mathbf{U}$ and an initial state $\mathbf{x}_0$, Euler integration is used to predict future states $\mathbf{x}_i$, $i \in 1\text{-}p$ using the nonlinear model $f(\mathbf{x},\mathbf{u})$, as follows:

$$\mathbf{x}_{i+1} = \mathbf{x}_i + t_s f(\mathbf{x}_i, \mathbf{u}_i) \tag{56}$$

The clearance from hazards $h(\mathbf{x}_i)$ and predicted threat for each threat source $J_k(\mathbf{x}_i,\mathbf{u}_i)$ are computed over the prediction horizon and ordered in vectors $\mathbf{h}$ and $\mathbf{J}_k$.

$$\mathbf{h} = \begin{bmatrix} h(\mathbf{x}_1) & h(\mathbf{x}_2) & \dots & h(\mathbf{x}_{p-1}) & h(\mathbf{x}_p) \end{bmatrix}^T \tag{57}$$

$$\mathbf{J}_k = \begin{bmatrix} J_k(\mathbf{x}_0,\mathbf{u}_0) & J_k(\mathbf{x}_1,\mathbf{u}_1) & \dots & J_k(\mathbf{x}_{p-1},\mathbf{u}_{p-1}) \end{bmatrix}^T \tag{58}$$

A practical challenge for threat prediction is the computational burden associated with long prediction horizons. The length of the prediction horizon is important, as the threat caused by hazards beyond the prediction horizon is not computed. If the prediction horizon is shorter than the sensor horizon, some sensory information is not used in the threat or control calculations. An approximation of vehicle behavior from the end of the prediction horizon to the maximum sensor range can be used to exploit this information. When used in an optimal control framework, this approximation is commonly known as the "cost-to-go."

For a controller with prediction horizon p, the cost-to-go is computed based on the final predicted state $\mathbf{x}_p$. To represent the effect of actuator dynamics on the cost-to-go, a time lag that consists of q prediction steps of duration t_s is introduced. The model is predicted forward to state $\mathbf{x}_{p+q}$ with zero input. This corresponds to a zero-order hold on the current steering and braking states. Note that the clearance vector $\mathbf{h}$ from (57) and threat vector $\mathbf{J}_k$ from (58) should be augmented for states $\mathbf{x}_{p+1}$ to $\mathbf{x}_{p+q}$.

The threat approximation based on simple maneuvers from the previous section is used as a "cost-to-go" for this model predictive controller. The cost-to-go $J_k^*(\mathbf{x}_{p+q})$ is based on the acceleration of simple maneuvers from the vehicle state at the end of the prediction horizon, as shown below.

$$J_k^*(\mathbf{x}_{p+q}) = \min\left\{ \frac{a_1}{a_{\max}}, \quad \frac{a_2}{a_{\max}}, \quad \frac{a_3}{a_{\max}} \right\} \tag{59}$$

The approximate threat from the end state $\mathbf{x}_p$ is denoted $J_k^*(\mathbf{x}_p)$. The approximate threat is incorporated into vector $\mathbf{J}_k^*$.

$$\mathbf{J}_k^* = \begin{bmatrix} J_k(\mathbf{x}_0,\mathbf{u}_0) & \dots & J_k(\mathbf{x}_{p+q-1},\mathbf{u}_{p+q-1}) & J_k^*(\mathbf{x}_{p+q}) \end{bmatrix}^T \tag{60}$$

The model predictive control problem is posed as a nonlinear program by incorporating predicted threat and approximate threat into an objective function used to determine the vector of optimal inputs $\mathbf{U}^*$, while enforcing inequality constraints.

$$\mathbf{U}^* = \arg\min_{\mathbf{U}} \max_k \left\| \mathbf{J}_k^* \right\|_\infty \tag{61}$$

$$\mathbf{h} \geq r \tag{62}$$

$$\left|\delta_i\right| \leq \delta_{\max} \quad i \in \{1..p\} \tag{63}$$

$$\left|u_{brake,i}\right| \leq u_{brake,\max} \quad i \in \{1..p\} \tag{64}$$

$$\left|\mathbf{u}_i\right| \leq \mathbf{u}_{\max} \quad i \in \{0..p-1\} \tag{65}$$

E. Threat-based control intervention

The final aspect of the proposed semi-autonomous hazard avoidance system is threat-based control intervention. After the nonlinear MPC controller has computed the optimal threat J^* and input sequence $\mathbf{U}^*$, an intervention level is determined based on the predicted threat. When threat is low, the controller intervention is kept low to maximize driver autonomy. As threat increases above a certain threshold, the system will begin to apply the optimal inputs from $\mathbf{U}^*$.

The intervention system reads the driver's current input $\mathbf{u}_{driver}$, the MPC input $\mathbf{u}_{mpc}$, and the predicted threat J^*. An intervention gain $K \in [0,1]$ is computed based on the predicted threat J^*, and is used to determine the applied inputs to the system according to the following equation:

$$\mathbf{u} = K\mathbf{u}_{driver} + (1-K)\mathbf{u}_{mpc} \tag{66}$$

The intervention gain K may be computed according to a variety of intervention laws, such as a linear function with or without deadband [17]. A switching intervention law with hysteresis is illustrated in Fig. 10 and given by the following equation:

$$K(t_i) = \begin{cases} 0 & K(t_{i-1}) = 0,\ J^*(t_i) \leq \Phi_{on} \\ 1 & K(t_{i-1}) = 0,\ J^*(t_i) > \Phi_{on} \\ 1 & K(t_{i-1}) = 1,\ J^*(t_i) \geq \Phi_{off} \\ 0 & K(t_{i-1}) = 1,\ J^*(t_i) < \Phi_{off} \end{cases} \tag{67}$$

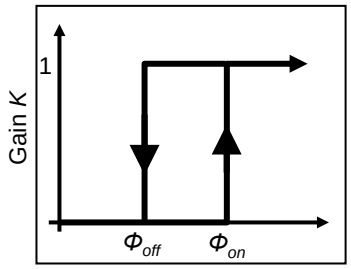

Fig. 10. Switching intervention law with hysteresis.

The use of hysteresis in the intervention function prevents small oscillations in the threat function from rapidly switching the intervention gain K. In practice, this causes the system to wait until threat has reduced below a specific level to return control authority to the driver.

III. Simulation and Experimental Results

This section presents results of the semi-autonomous hazard avoidance system in simulation and experiments. A numerical implementation of the MPC controller is described, including a discussion of the effect of prediction horizon length. Hazard avoidance results are then presented from simulation and experiments.

A. Implementation of MPC controller

The minimum threat MPC controller was implemented using the nonlinear optimization package NPSOL. NPSOL uses a sequential quadratic programming algorithm to minimize a smooth nonlinear objective function subject to linear and nonlinear constraints [22]. The solver has the capability to use gradients of the cost and constraint functions to speed convergence. Symbolic derivatives are used in the model prediction, cost function, and constraints of the MPC controller to improve performance.

The prediction horizon length is widely acknowledged to be a critical parameter in the design of model predictive controllers. A long prediction horizon may improve controller stability and performance, though it also increases the computational demand of the controller. A challenge of algorithms based on numerical optimization is avoiding local minima in non-convex problems. The optimization will converge to a solution that depends on the initial guess of the optimal control vector $\mathbf{U}^*$. It has been observed in this work that it is more challenging to determine initial guesses that converge to the global minimum for MPC controllers with longer prediction horizons (and hence more control variables) than for controllers with shorter prediction horizons.

An example of this phenomenon is illustrated in Fig. 11. An MPC controller with p=30, q=1, and t_s = 0.05 s is solved with three different initial guesses to the optimal control vector $\mathbf{U}^*$. These initial guesses result in a stopping maneuver with cost 0.399 and two symmetric passing maneuvers with cost 0.305.

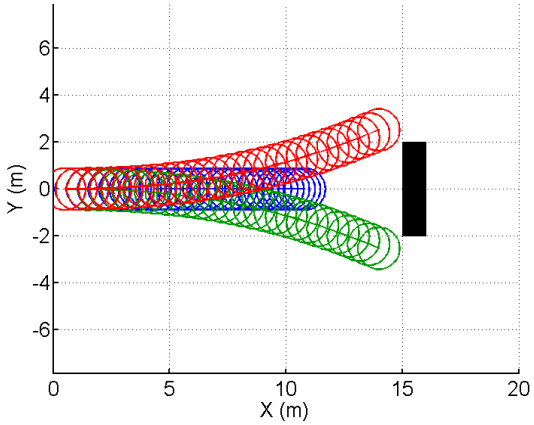

Fig. 11. Multiple solutions to MPC control law with p=30, q=1, and t_s=0.05s representing separate local minima.

It has already been noted that the use of cost-to-go with a short prediction horizon can approximate the performance of an MPC controller with much longer prediction horizon, though with the benefit of a reduced computational demand. An additional advantage is the reduced size of the optimization vector $\mathbf{U}^*$, which reduces the challenge associated with local minima and sensitivity to initial guess of the optimization vector $\mathbf{U}^*$. For these reasons, the MPC controller parameters used in these results are based on a prediction horizon of p=1. The parameter values q=4 and t_s=0.05 s were chosen based on the properties of the model and required computational time of the MPC controller.

While the vehicle model described in Section II.A. may use a nonlinear tire model, the model used in these results is linear. The model is described by the equations below with parameters C_f=68 kN/rad and C_r=87 kN/rad referred to as the tire cornering stiffnesses. This tire model is suitable for small levels of tire slip and requires one parameter, while other tire models require many tire parameters, increasing the burden of model matching.

$$F_{yf} = -C_f \alpha_f \tag{68}$$

$$F_{yr} = -C_r \alpha_r \tag{69}$$

It should be noted that the slip angle is undefined at zero speed. As such, all simulations are aborted when the vehicle speed drops below a threshold of 0.5 m/s.

B. Experimental setup

Experimental testing was performed using a 2001 Jaguar S-Type passenger vehicle operated by several human drivers. Driver and actuator steering inputs were coupled via an Active Front Steer (AFS) system. An inertial and GPS navigation system was used to measure vehicle position, sideslip, yaw angle, and yaw rate. Cones were placed in the driving environment to represent hazards, and their location was encoded in the controller as GPS coordinates. A 1 GHz dSPACE™ processor ran controller code and interfaced with steering and braking actuators. With the short prediction horizon and computationally-efficient cost-to-go computation, the controller calculations remained within a 50 ms sampling time.

The test setup for both the simulations and experiments involved defining a hazard edge in the environment and approaching the edge from a variety of initial conditions. The cost-to-go was computed based on the type of avoidance trajectory that required the minimum level of threat. The preference for different trajectories depends on the hazard location and orientation relative to the vehicle.

A passing maneuver was tested by approaching a hazard face perpendicular to the direction of travel and near the edge, as in Part *A* of Fig. 5. A stopping maneuver was tested by approaching a hazard face perpendicular to the direction of travel and far from the edges, as in Part *B* of Fig. 5. A non-passing turn was tested by approaching a hazard face with a large skew angle and far from the edges, as in Part *C* of Fig. 5.

C. Stopping maneuver

A stopping maneuver was demonstrated by approaching a wide hazard perpendicular to the vehicle direction of travel. Two separate tests were conducted to verify the functionality of the hazard avoidance system. In the first test, a human driver initiates braking to avoid the hazard before the threat exceeded the threshold Φ_{on}. This test demonstrates the driver's freedom to operate the vehicle in low-threat situations. In the second test, the human driver approaches the hazard without engaging the brakes so that the vehicle automatically engages the brakes once the threat exceeds the threshold Φ_{on}.

Results from the stopping test without controller intervention are given in Fig. 12-13. The driver stopped the vehicle before the predicted threat threshold was exceeded.

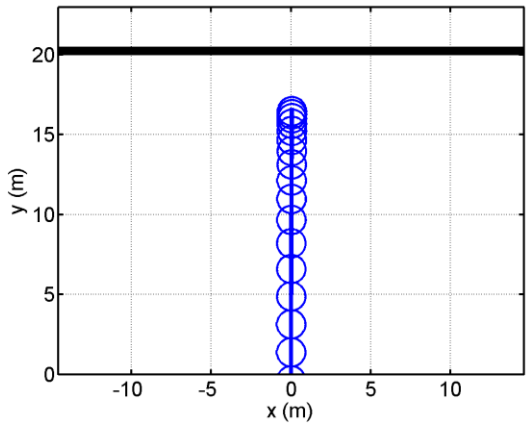

Fig. 12. Vehicle path during stopping maneuver initiated by driver without controller intervention. The critical hazard edge is wide and perpendicular to the vehicle direction of travel. The vehicle path is illustrated by the circles.

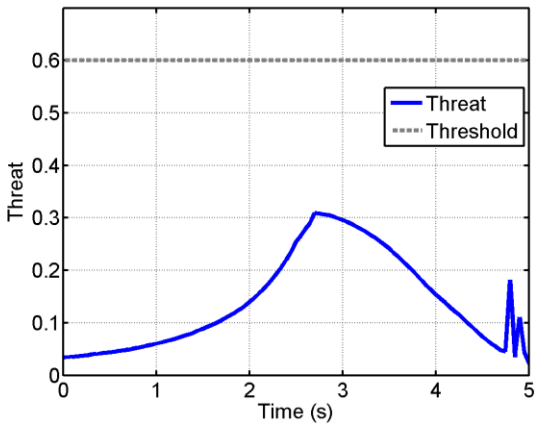

Fig. 13. Predicted threat during stopping maneuver initiated by driver without controller intervention. The threat did not exceed the threshold, so the controller did not intervene.

Results of a stopping maneuver with controller intervention are presented below based on simulated and experimental data. Neither the simulated driver nor the human driver in the experiment engaged the brakes and both maintained a constant steering angle. The initial vehicle speed was approximately 8 m/s and the threat threshold was Φ_{on} = 0.3. The path, threat, speed, and acceleration from simulation and experiment are presented in Fig. 14-17. Note that the threat threshold was exceeded at approximately 0.68 s. This is indicated as a solid vertical line labeled "Engage" in Fig. 15-17.

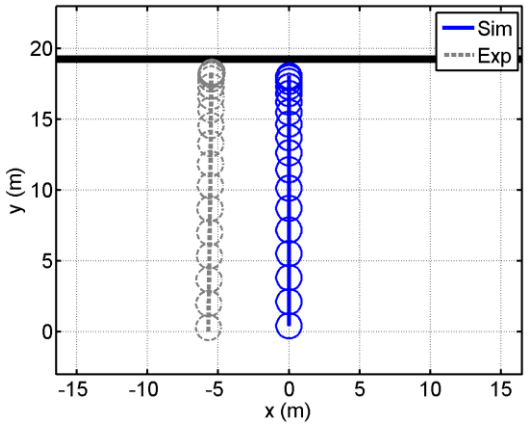

Fig. 14. Paths during stopping maneuver at 8 m/s with Φ_{on} = 0.3. The critical hazard edge is wide and perpendicular to the vehicle direction of travel. The vehicle path is illustrated by the circles. The simulated path is on the right with solid lines, while the experimental path is on the left with dashed lines.

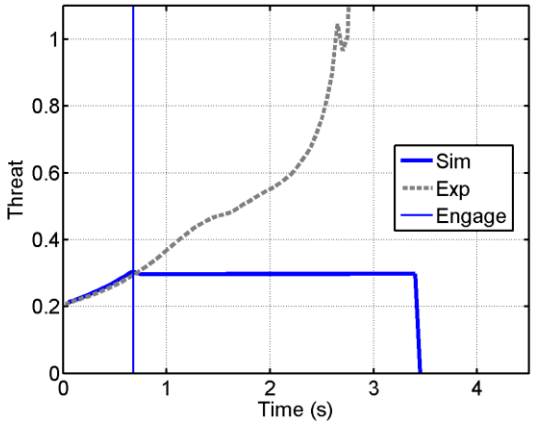

Fig. 15. Predicted threat during stopping maneuver at 8 m/s with Φ_{on} = 0.3.

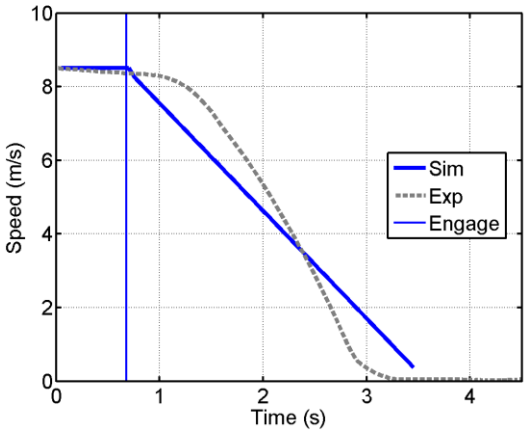

Fig. 16. Vehicle speed during stopping maneuver at 8 m/s with Φ_{on} = 0.3.

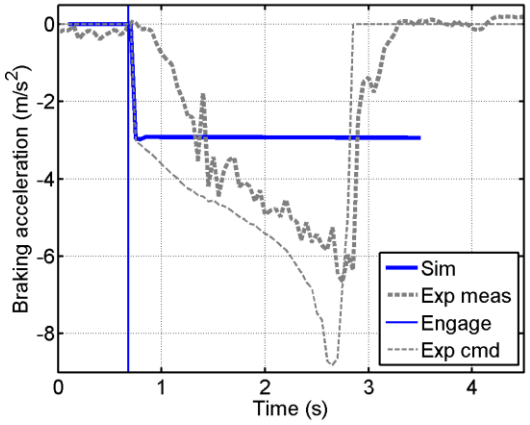

Fig. 17. Vehicle braking acceleration during stopping maneuver at 8 m/s with Φ_{on} = 0.3. The simulated acceleration is denoted by "Sim" and the commanded and measured accelerations from the experiment are denoted "Exp cmd" and "Exp meas" respectively.

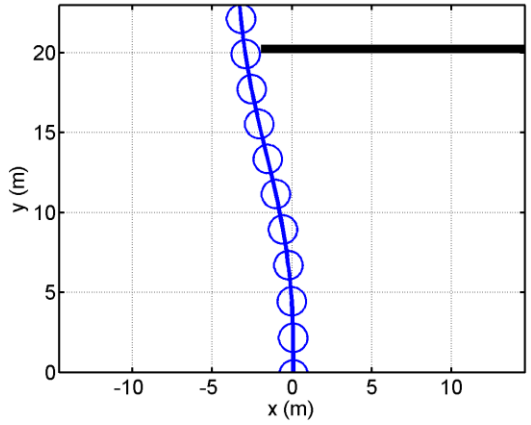

Fig. 18. Vehicle path during passing maneuver initiated by driver without controller intervention. The vehicle is near a corner of the hazard and travels perpendicular to the hazard face. The vehicle path is illustrated by the circles.

The simulated vehicle slowed before the hazard edge until the minimum simulation speed of 0.5 m/s was reached. The initial threat was approximately 0.2 and reached the threshold value of Φ_{on} = 0.3 at approximately 0.68 s. After reaching the predicted threat threshold, the simulated vehicle applied braking quickly and held the predicted threat roughly constant for the duration of the maneuver.

The initial threat and acceleration command for the experimental vehicle matched the simulation data, though a significant lag was observed between the braking command and the measurement of deceleration. This led to an increase in both threat and the braking command magnitude. The vehicle reached the face of the virtual obstacle with a speed of about 1 m/s before stopping 0.2 m past the cones. The controller performance during this test is discussed further in section IV.

D. Passing turn

A passing turn was demonstrated by approaching a hazard corner perpendicular to the hazard face. Similar to the stopping maneuver, tests without controller intervention and with controller intervention are presented.

Results from the passing maneuver without controller intervention are presented in Fig. 18-19. The initial speed was 12 m/s with threshold Φ_{on} = 0.6. The driver initiated a passing maneuver and successfully avoided the obstacle.

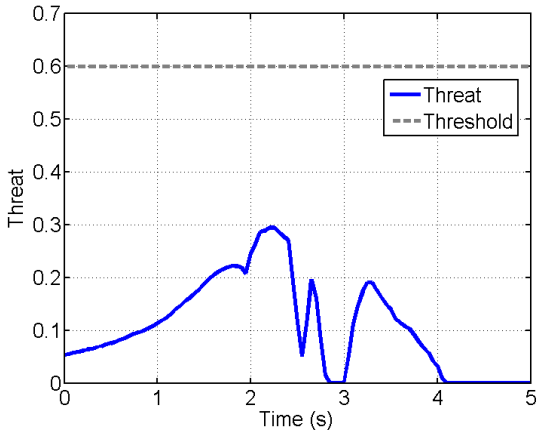

Fig. 19. Predicted threat during passing maneuver initiated by driver without intended controller intervention.

Results from the passing maneuver with controller intervention are presented below. Neither the simulated driver nor the human driver engaged the brakes and both maintained a constant steering angle. The vehicle speed began at approximately 13 m/s and the threat threshold was Φ_{on} = 0.3. The path, threat, speed, and acceleration are presented in Fig. 20-23. The time when the threat threshold was crossed is indicated by a solid vertical line labeled "Engage" in Fig. 21-23.

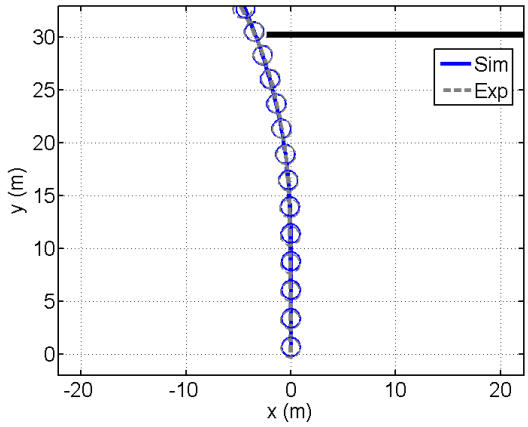

Fig. 20. Paths during passing maneuver at 13 m/s with Φ_{on} = 0.3. The vehicle is near a corner of the hazard and travels perpendicular to the hazard face. The vehicle path is illustrated by the circles.

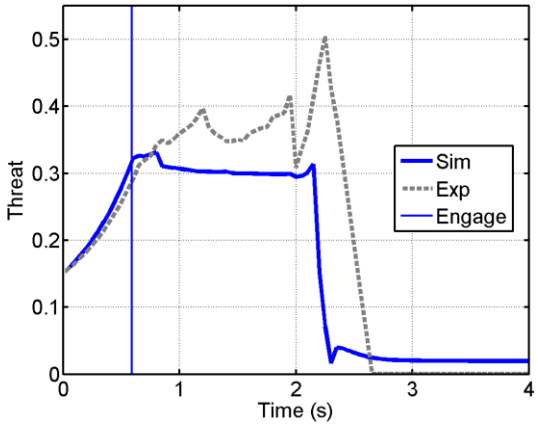

Fig. 21. Predicted threat during passing turn at 13 m/s with Φ_{on} = 0.3.

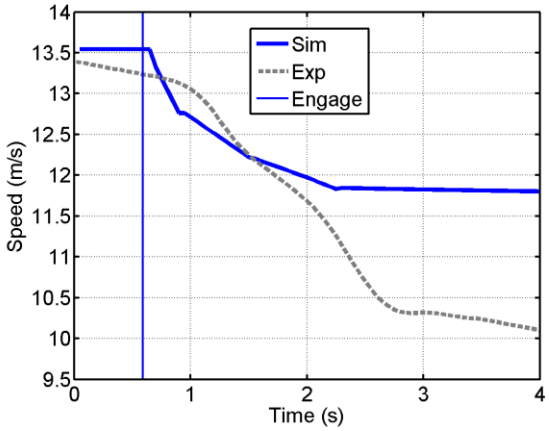

Fig. 22. Vehicle speed during passing turn at 13 m/s with Φ_{on} = 0.3.

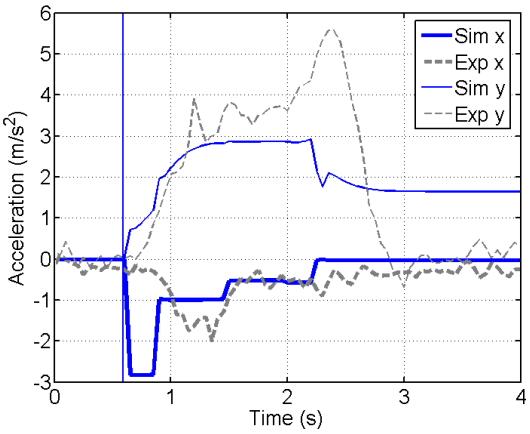

Fig. 23. Vehicle acceleration during passing turn at 13 m/s with Φ_{on} = 0.3. The longitudinal and lateral directions are denoted by *x* and *y* respectively.

The initial threat was 0.15 and increased to the threshold of Φ_{on} = 0.3 at approximately 0.59 s. After reaching the threshold, both the simulated and experimental vehicles applied a combination of braking and steering inputs to avoid the hazard. There is a close match between the simulated and experimental vehicle paths shown in Fig. 20. The simulated threat reached a peak of 0.33 and remained roughly constant during the maneuver. The experimental threat reached a peak of 0.50. The differences between the simulated and experimental threat may be caused by model parameter mismatch.

E. Non-passing turn

A non-passing maneuver was demonstrated with a single experimental result with controller intervention. This maneuver was tested by defining a very long hazard edge nearly parallel to the vehicle's direction of travel. This scenario corresponds to a lane-keeping task or prevention of road departure. The path and threat of the maneuver are given in Fig. 24-25. The initial speed of the vehicle was 21 m/s with a threshold of Φ_{on} = 0.3.

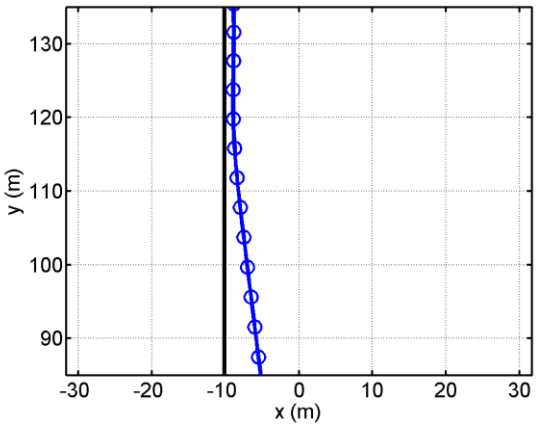

Fig. 24. Experimental demonstration of non-passing turn with 1-step prediction and cost-to-go. The critical hazard edge is long and nearly parallel to the vehicle direction of travel. The vehicle path is illustrated by the circles.

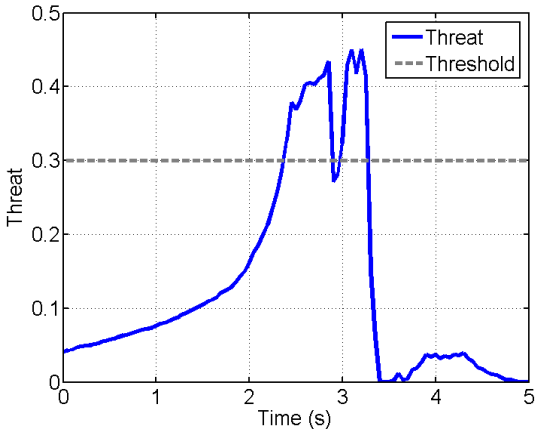

Fig. 25. Predicted threat during non-passing turn maneuver initiated by controller intervention.

IV. Discussion

The semi-autonomous hazard avoidance system was demonstrated experimentally for stopping, passing turn, and non-passing turn maneuvers with and without driver intervention. The use of the short prediction horizon with cost-to-go enabled the nonlinear MPC computation to be completed within 50 ms and the controller to run in real-time. During these tests, there were no instances of computation overrunning the allotted computation time.

The semi-autonomous nature of the system was demonstrated successfully in low-threat situations when the driver took action to avoid the hazard and the system did not intervene. The intervention behavior of the semi-autonomous system can accommodate varying levels of driver skill by adjusting the threat threshold parameter Φ_{on}.

The semi-autonomous nature of the system was also demonstrated successfully in high-threat situations for passing and non-passing turns when the system engaged the steering and braking actuators to successfully avoid the hazard. The vehicle did not stop completely before the hazard face during the stopping test, however. Comparing the simulation results to the experimental results, a significant lag was observed between the commanded and actual braking deceleration. This is likely caused by unmodeled lag in the braking actuator dynamics. It is well known that model mismatch can cause problems for nonlinear model predictive control. Future work with model predictive control for hazard avoidance via braking should consider the effect of braking actuator dynamics on system performance.

V. Conclusion

A hazard avoidance controller based on a minimum threat model predictive controller was presented and demonstrated in simulations and experiments. An approximation of threat based on computationally efficient analytical calculations of canonical avoidance maneuvers was used as a cost-to-go to reduce the computational demand. The system was found to successfully avoid hazards with passing and non-passing turns, though unmodeled lag in braking actuator dynamics caused performance problems in stopping maneuvers. Future work will attempt to address issues of model mismatch. Further work is needed before this research is road-ready.

Acknowledgment

The authors would like to thank Mitch McConnell, Dorian Spero, Jim Martell, Alex Miller, Tony Sleath, Gurunath Vemulakonda, Matt Rupp, Tim Zwicky, Jianbo Lu, Chris Teslak, Reid Steiger, and Jamil Alwan, all of Ford Motor Co. for their assistance in conducting these experiments.

References

[1] C. M. Farmer, A. K. Lund, "Trends Over Time in the Risk of Driver Death: What If Vehicle Designs Had Not Improved?" *Traffic Injury Prevention*, v. 7, n. 4, pp. 335-342, December 2006.

[2] C. Farmer, "Effect of Electronic Stability Control on Automobile Crash Risk," *Traffic Injury Prevention*, v. 5, n. 4, pp. 317-325, 2004.

[3] National Highway Traffic Safety Administration, *Traffic Safety Facts 2004: A compilation of motor vehicle crash data from the FARS and the GES* (DOT HS 809 919), Washington, DC: National Highway Traffic Safety Administration, 2006.

[4] L. Evans, "The dominant role of driver behavior in traffic safety," *American Journal of Public Health*, v. 86, n. 6, pp. 784-786, 1996.

[5] M. Montemerlo, et al., "Junior: The Stanford entry in the Urban Challenge," *Journal of Field Robotics*, v. 25, n. 9, pp. 569-597, 2008.

[6] C. Urmson, et al., "Autonomous driving in urban environments: Boss and the Urban Challenge," *Journal of Field Robotics*, v. 25, n. 8, pp. 425-466, 2008.

[7] M. Buehler, K. Iagnemma, S. Singh, (eds.) *The 2005 DARPA Grand Challenge: The Great Robot Race*, Springer Tracts in Advanced Robotics (STAR) Series, v. 36, Springer, August, 2007.

[8] S. Ashley, "Driving Toward Crashless Cars," *Scientific American*, v. 299, n. 6, pp. 86-94, Dec. 2008.

[9] J.P. Switkes, E.J. Rossetter, I.A. Coe, J.C. Gerdes, "Handwheel Force Feedback for Lanekeeping Assistance: Combined Dynamics and Stability," *Journal of Dynamic Systems, Measurement, and Control*, v. 128, n. 3, pp. 532--542, 2006.

[10] E. J. Rossetter, C. J. Gerdes, "Lyapunov Based Performance Guarantees for the Potential Field Lane-keeping Assistance System," *Journal of Dynamic Systems, Measurement, and Control*, v. 128, n. 3, pp. 510-522, 2006.

[11] T. Sattel, T. Brandt, "From robotics to automotive: Lane-keeping and collision avoidance based on elastic bands," *Vehicle System Dynamics*, v. 46, n. 7, pp. 597-619, 2008.

[12] M. Spenko, Y. Kuroda, S. Dubowsky, K. Iagnemma, "Hazard Avoidance for High Speed Unmanned Ground Vehicles in Rough Terrain," *Journal of Field Robotics*, v. 23, n. 5, pp. 311-331, May 2006.

[13] A. Richards, Y. Kuwata, J. How, "Experimental Demonstrations of Real-Time MILP Control," *Proc. AIAA Guidance, Navigation, and Control Conference and Exhibit*, Aug. 11-14 2003, n. AIAA-2003-5802.

[14] A.J. Eele, A.G. Richards, "Path-Planning with Avoidance Using Nonlinear Branch-and-Bound Optimization," *AIAA Journal of Guidance, Control and Dynamics*, v. 32, n. 2, pp. 384-394, March 2009.

[15] P. Falcone, F. Borrelli, J. Asgari, H. E. Tseng, D. Hrovat, "Predictive Active Steering Control for Autonomous Vehicle Systems," *IEEE Trans. Control Systems Technology*, v. 15, n. 3, pp. 566–580, 2007.

[16] S. Anderson, S. Peters, T. Pilutti, K. Iagnemma, "Experimental Study of an Optimal-Control-Based Framework for Trajectory Planning, Threat Assessment, and Semi-Autonomous Control of Passenger Vehicles in Hazard Avoidance Scenarios," *Proceedings of the 2009 Conference on Field and Service Robots*, 2009.

[17] S. Anderson, S. Peters, T. Pilutti, K. Iagnemma, "An Optimal-Control-Based Framework for Trajectory Planning, Threat Assessment, and Semi-Autonomous Control of Passenger Vehicles in Hazard Avoidance

Scenarios," *International Journal of Vehicle Autonomous Systems*, v. 8, n. 2/3/4, pp. 190-216, 2010.

[18] G. Engelman, et al., "Threat level identification and quantifying system," U.S. Patent 7,034,668, Apr. 25, 2006.

[19] S. J Anderson, "A Unified Framework for Trajectory Planning, Threat Assessment, and Semi-Autonomous Control of Passenger Vehicles," Master's thesis, Massachusetts Institute of Technology. Dept. of Mechanical Engineering, Cambridge, MA, June 2009.

[20] Jurgen Ackermann, "Robust decoupling, ideal steering dynamics and yaw stabilization of 4WS cars," *Automatica*, v. 30, n. 11, pp. 1761-1768, November 1994.

[21] S. J Anderson, S. Peters, T. Pilutti, H. E. Tseng, K. Iagnemma, "Semi-autonomous Avoidance of Moving Hazards for Passenger Vehicles," Proceedings of the ASME Dynamic Systems and Control Conference, 2010.

[22] P. E. Gill, W. Murray, M. A. Saunders, and M. H. Wright, "User's guide for NPSOL 5.0: a Fortran package for nonlinear programming," Report SOL 86-1, Department of Operations Research, Stanford University, Stanford, CA, 1986.

First A. Author (M'76–SM'81–F'87) and the other authors may include biographies at the end of regular papers. Biographies are often not included in conference-related papers. This author became a Member (M) of IEEE in 1976, a Senior Member (SM) in 1981, and a Fellow (F) in 1987. The first paragraph may contain a place and/or date of birth (list place, then date). Next, the author's educational background is listed. The degrees should be listed with type of degree in what field, which institution, city, state, and country, and year degree was earned. The author's major field of study should be lower-cased.

The second paragraph uses the pronoun of the person (he or she) and not the author's last name. It lists military and work experience, including summer and fellowship jobs. Job titles are capitalized. The current job must have a location; previous positions may be listed without one. Information concerning previous publications may be included. Try not to list more than three books or published articles. The format for listing publishers of a book within the biography is: title of book (city, state: publisher name, year) similar to a reference. Current and previous research interests end the paragraph.

The third paragraph begins with the author's title and last name (e.g., Dr. Smith, Prof. Jones, Mr. Kajor, Ms. Hunter). List any memberships in professional societies other than the IEEE. Finally, list any awards and work for IEEE committees and publications. If a photograph is provided, the biography will be indented around it. The photograph is placed at the top left of the biography. Personal hobbies will be deleted from the biography.